Article:

Wang, X, Santos-Carballal, D orcid.org/0000-0002-3199-9588 and De Leeuw, NH orcid.org/0000-0002-8271-0545 (2021) Density Functional Theory Study of Monoclinic FeNbO4: Bulk Properties and Water Dissociation at the (010), (011), (110), and (111) Surfaces. Journal of Physical Chemistry C, 125 (50). pp. 27566-27577. ISSN 1932-7447

https://doi.org/10.1021/acs.jpcc.1c05452

A Density Functional Theory Study of Monoclinic $FeNbO_4$: Bulk Properties and Water Dissociation at the (010), (011), (110) and (111) Surfaces

Xingyu Wang,[1] David Santos-Carballal,[1] and Nora H. de Leeuw[1,2*]

1. School of Chemistry, University of Leeds, Leeds LS2 9JT, United Kingdom
2. School of Chemistry, Cardiff University, Cardiff CF10 3AT, United Kingdom

Keywords: DFT calculations, monoclinic $FeNbO_4$, Bulk properties, Surface morphology, Water dissociation.

Abstract

Monoclinic and orthorhombic $FeNbO_4$-based materials have been developed for many applications, including as hydrogen sensors and solid oxide electrolysis cell (SOEC) electrodes. Here, we have employed density functional theory (DFT) calculations to investigate the bulk and surface properties of the monoclinic $FeNbO_4$ structure, as well as water adsorption and dissociation on its pristine surfaces. Our calculations show that the high spin state Fe^{3+} cations have a relatively smaller Bader charge than the Nb^{5+} cations, which accounts for Nb-O bonds that are stronger than the Fe-O bonds. The analysis of the density of states (DOS) shows that the O 2p orbital occupies most of valence band, including its maximum (VBM), with negligible contributions from the 4d and 3d orbitals of Nb and Fe cations, respectively. We found that the 3d orbitals of Fe occupy the conduction band minimum (CBM), which explains that electrons are conducted via the Fe-O-Fe framework. The calculation of the elastic constants demonstrates that pure monoclinic $FeNbO_4$ is mechanically stable. We have also considered the thermodynamic stability and structures of the seven low Miller-index surfaces and found that the (010) facet has the lowest surface energy and expresses the largest area in the Wulff crystal shape of the particle. Finally, we have simulated the interaction of water with the Fe^{3+} and Nb^{5+} sites of the four most stable surfaces and found that the dissociative adsorption of water takes place only on the (110) surface, which has important implications for the

use of this material as a SOEC electrode.

Introduction

In recent years, research has intensified into the development of the ABO_4-type oxides, including iron niobate ($FeNbO_4$)[1-6]. So far, three different $FeNbO_4$ phases have been reported, i.e. the monoclinic wolframite-type structure (m-$FeNbO_4$, space group P2/c), the orthorhombic α-PbO_2-type structure (o-$FeNbO_4$, space group P2/c) and the rutile-type structure (r-$FeNbO_4$, space group P42/mnm)[7]. Under ambient conditions, m-$FeNbO_4$ has the most stable structure,[7-8] where both Fe^{3+} and Nb^{5+} are coordinated by six oxygen ions, forming stable octahedra. In addition, the Fe^{3+} and Nb^{5+} cations are distributed in an ordered fashion along zig-zag chains of [FeO_6] and [NbO_6] octahedra.[8] The m-$FeNbO_4$ phase is stable up to 1050 ℃,[7] which is the temperature at which the cation distribution becomes disordered. The complete phase transformation is observed near 1100 ℃ with the resulting materials showing a typical α-PbO2 and rutile-type structure in the range of temperatures 1100 - 1380 ℃ and 1380 -1450 ℃, respectively [7-9].

Out of the three iron niobate phases, m- and o-$FeNbO_4$ are promising materials for many applications. For example, m-$FeNbO_4$ has excellent potential as a gas sensor material[10-12], owing to its good electrical properties due to the similar radii but different valence states of the Fe and Nb cations, whereas o-$FeNbO_4$ has been investigated as a photodetector for solar energy conversion devices[13-15] and an anode material in solid oxide fuel cells (SOFC)[2, 16]. Conventionally, nickel metal particle-based materials have been used widely in the cathodes of solid oxide electrolysis cells (SOEC) owing to their significant advantages, i.e. low cost, good catalytic ability and high electronic conductivity[17-19], although they also have disadvantages, such as coarsening and depletion of Ni particles[20-21]. In order to improve the stability of the cathode, suitable ABO_3 perovskites are being explored as replacements for the Ni metal, or other metals are introduced form more stable alloys with Ni[18-20]. Interestingly, both m- and o-$FeNbO_4$ have shown potential as replacement materials for the Ni metal, owing to their proven catalytic efficacy and anti-depletion properties in the cathodes of SOEC[5], where the splitting of water vapor takes place.

However, no computational studies have been carried out on the surface properties and reactions with gases, especially the water vapor splitting, of the m- and o-$FeNbO_4$ phases. In this work, we have employed density functional theory (DFT) methods to study the bulk and surface properties, as well as water molecule adsorption and its dissociation reaction, on the m-$FeNbO_4$ material.

Computational methods

In this study, all DFT calculations were carried out using the Vienna Ab initio Simulations Package, VASP (version 5.4.4)[22-25]. The projector-augmented wave method (PAW)[26] and the generalized gradient approximation (GGA)[27] with the Perdew-Burke-Ernzerhof (PBE) density functional were used to describe the ion-electron interaction and the exchange-correlation interaction, respectively. All calculations were performed using spin-polarization and we have treated the following as valence electrons: Fe($3p^6 3d^7 4s^1$), Nb($4p^6 5s^1 4d^4 4s^2$), O($2s^2 2p^6$) and H(1s). To describe the electronic structures, we have used the on-site Coulombic interaction (DFT+U)[28] for the Fe 3d electrons with an U-J value of 4.3 eV. Following a series of test calculations, the kinetic energy cutoff for the plane wave basis was set at 500 eV. The Henkelman algorithm was used to calculate Bader charges.[29]

The $FeNbO_4$ bulk unit cell used in this work is the 1x1x1 P/2c monoclinic cell and the surface models were obtained using METADISE [30]. After cleaving the surfaces, we relaxed the top half of the atom layers and kept the bottom half of layers fixed at their bulk positions. The surface energies of the relaxed (γ_r) and unrelaxed (γ_u) systems can be obtained through the following equations[31-34]:

$$\gamma_u = \frac{E_{slab,u} - E_{bulk}}{2A} \quad (1)$$

$$\gamma_r + \gamma_u = \frac{E_{slab,r} - E_{bulk}}{A} \quad (2)$$

Where $E_{slab,u}$ and $E_{slab,r}$ refer to the total energy of the unrelaxed and half-relaxed slabs, respectively; E_{bulk} refers to the energy of the bulk containing the same number of formula units as the surface; A refers to the surface area of one side of the slab. In addition, 6x6x6, 4x4x1 and 1x1x1 gamma-centered Monkhorst Pack grids were used for the simulation of the bulk, surface slabs and isolated water molecule, respectively. The water molecule was modelled inside a large box of 10x10x10 $Å^3$.

All calculations of the bulk and surface and the water adsorption and dissociation reaction were performed with the conjugate gradients method with a convergence criterion of 0.01 eV/Å. For the adsorption calculations, we added a single water molecule above the pristine surfaces. In addition, we employed the climbing image nudge elastic band (CI-NEB) method[35] to study the transition states between the molecular adsorption and the dissociated states of water. For the transition states, we inserted four images along the minimum energy path (MEP) to calculate the saddle points, where the calculations were carried out using the limited memory Broyden Fletcher Goldfarb Shanno (LBFGS) method[36] until the forces were smaller than 0.05 eV/Å. We confirmed that each transition state has an imaginary vibrational frequency along the reaction direction.

The variation of the Helmholtz free energy (ΔF) in the process of adsorption and dissociation can be expressed as:

$$\Delta F = \Delta E - T\Delta S \quad (3)$$

where ΔE is the change in energy, T is the temperature and ΔS is the change in entropy.

For a solid phase, ΔF can be calculated as:[37-38]

$$\Delta F = \Delta E_{DFT} + \Delta E_{ZPE} - T\Delta S \quad (4)$$

where ΔE_{DFT}, ΔE_{ZPE}, and ΔS are the variation of the electronic energy obtained from the DFT calculations, the zero-point energy correction, and the vibrational contribution to the entropy, respectively. In this work, ΔE_{ZPE} and ΔS have been obtained by calculating the vibrational frequencies, as shown in the ESI. The thermodynamic data for gaseous H_2O are obtained from experimental data.[39]

The ΔE_{DFT} for the adsorption and dissociation of H_2O on the surfaces can be expressed as:

$$\Delta E_{DFT} = E_{sur + adsorbate} - (E_{sur} + E_{H_2O}) \qquad (5)$$

where $E_{sur + adsorbate}$ represents the total energy of the surface-adsorbate system, E_{sur} represents the total energy of the pristine surface and E_{H_2O} represents the energy of the isolated H_2O molecule. In this work the adsorption free energy was calculated at the representative temperatures of 0, 300 and 600 K under a pressure of 1 atmosphere. Once adsorbed at the surfaces, the water molecule is treated as a part of the solid phase.

The equilibrium morphology of a $FeNbO_4$ particle was constructed by means of the Wulff method, where the free energy of a given surface is proportional to the distance from the center of the polyhedron to that surface[40]. Under the conditions of our calculations, i.e. at 0 K and in the absence of oxygen vapor, the surface energy obtained through static calculations is equal to the surface free energy (σ(T, p)), since the surface slab has the same stoichiometry of the bulk. This method has been shown to describe successfully particle morphologies of many materials[31, 41-44]. The scanning tunnelling microscopy (STM) images of the exposed surfaces of $FeNbO_4$ were calculated using the Tersoff-Hamman approach as implemented in HIVE[45]. We selected a range from -1.7 eV to the Fermi level to integrate the partial charge density of the STM images.

Results and Discussion

Bulk Properties

The structural parameters of $FeNbO_4$ after optimization are listed in Table 1. The computational prediction of the lattice parameters compares very well with the experimental values, as the deviation is within 1.5 %. The optimized β angle is not 90 ° (90.4 °), again in agreement with the conditions of a monoclinic structure, and has the same value as in experimental reports (90.4 °), and the bond lengths are shown in Figure 1.

Table 1 Lattice parameters of $FeNbO_4$ and related interatomic distances after optimization

	Fe-O (Å)	Nb-O(Å)	a (Å)	b (Å)	c (Å)	α (°)	β (°)	γ (°)
Simulated	2.030	2.170	4.687	5.691	5.038	90	90.4	90
(experiments)[10]	(2.014)	(2.161)	(4.637)	(5.607)	(4.992)	(90)	(90.1)	(90)
	1.997	1.981						
	(1.927)	(2.008)						
	2.109	1.901						
	(2.115)	(1.858)						

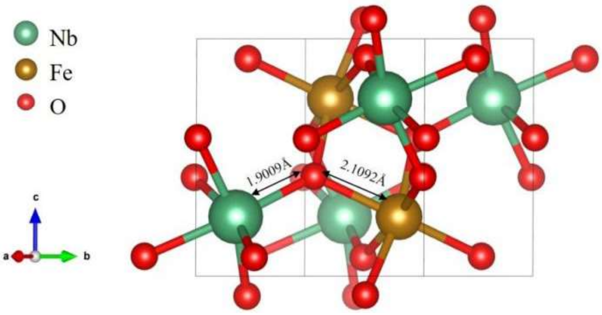

Figure 1 Lattice structure of $FeNbO_4$ after optimization.

Furthermore, we have employed an initial high-spin electron distribution for the Fe^{3+} cations (5.2 μ_B) to study the effect of different spin configurations on the magnetization properties of the bulk. We have set up a 2x2x2 supercell, where we considered two antiferromagnetic configurations and the ferromagnetic structure, which are denoted as AFM1, AFM2, and FM, respectively. As shown in Figure 2, adjacent Fe^{3+} layers perpendicular to the [100] direction have antiparallel spin orientation in AFM1, whereas AFM2, in contrast, is characterised by antiparallel spin orientation within each Fe^{3+} layer. For the FM configuration all Fe^{3+} cations have the same spin orientation. The calculated bulk properties are listed in Table S1, which shows that the effect of the magnetic ordering on the lattice parameters, the atomic Bader charges (q) and magnetic moments (μ) are insignificant for $FeNbO_4$. Specifically, as expected Nb atoms lose more electrons than Fe and thus form stronger bonds with O. The Fe cations have a large calculated value of 4.27 μ_B, which is close to experiment (4.66 μ_B)[46], indicating that these cations are in a high spin state, in both spin channels. Unlike the Fe cations, Nb loses all of its 4d valence electrons and thus has a very low, almost zero value of μ. Remarkably, the ground state energy differences of these three types of magnetic spin configurations for m-$FeNbO_4$ are negligible (maximum ~0.04 eV/unit cell), that even if we were to take the AFM1 structure as the most stable structure, in agreement with earlier assumptions[46-48], it is likely that there will be a mixture of the three magnetic structures occurring, potentially in different domains of the material.

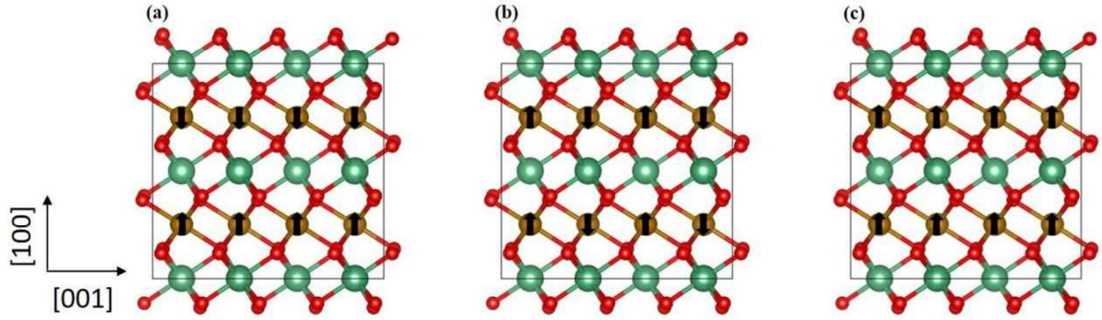

Figure 2 Three different magnetic structures for m-FeNbO$_4$; (a): antiferromagnetic structure 1 (AFM1); (b): antiferromagnetic structure 2 (AFM2); (c): ferromagnetic structure (FM);

The PDOS plots of the three magnetic structures of m-FeNbO$_4$ are shown in Figure 3, where the distribution of bands near the valence band maximum (VBM) and the conduction band minimum (CBM) as well as their band gap energy (~2 eV) are very similar, which is very close to the experimental value (1.81-2.2 eV)[47]. In all three phases, the O 2p orbital occupies almost the entire valence band, including its maximum (CBM) with negligible contribution from the Nb and Fe cations. Moreover, the t_{2g} and e_g orbitals of Fe (3d) occupy most of the β channel of spins of the conduction band, including the conduction band minimum (CBM), with minor contribution in the α channel. The t_{2g} and e_g orbitals of Nb (4d) mostly occupy both the α and β channels in the conduction band far from the CBM. This result is consistent with the high and low spin state of the Fe and Nb ions, respectively. In addition, both the Fe and Nb t_{2g} orbitals occupy a larger area than the e_g orbitals in the conduction band, showing the distribution priority of electrons when there is a charge transfer process. So far, our results suggest that the electron conduction mechanism involves a promotion from the O 2p (VBM) to the Fe 3d orbitals (CBM), i.e. in the Fe-O-Fe framework, which corresponds to experimental results[48].We have also demonstrated that the spin configuration have a minimal impact on the bulk properties of the material and therefore subsequent calculations were carried out using the FM phase for the sake of simplicity.

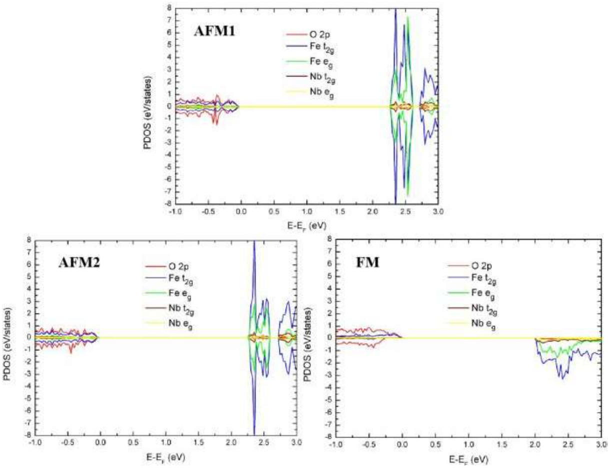

Figure 3 Projected of the total density states (PDOS) for the Fe, Nb and O in the AFM1, AFM2, and FM phase.

Finally, we have calculated the elastic constants C_{ij} where the finite difference technique was employed to determine the elastic tensor by performing finite distortions in the direction of each Cartesian coordinate of the lattice and deriving C_{ij} through the stress-strain method as:[49-50]

$$C_{ij} = \frac{1}{V} \frac{\partial^2 E}{\partial \varepsilon_i \partial \varepsilon_j} \quad (6)$$

where E is the total energy of the stressed cell, V is the equilibrium volume and ε is the component of the applied strain. For the AFM1, AFM2, and FM spin configurations of $FeNbO_4$, there are 13 independent elastic constants (C_{11}, C_{22}, C_{33}, C_{44}, C_{55}, C_{66}, C_{12}, C_{13}, C_{23}, C_{15}, C_{25}, C_{35} and C_{46}), which are listed in Table S2. It is clear that the elastic constants for the three phases are virtually the same, demonstrating that the spin orientation has a negligible influence on the mechanical properties.

The twelve stability criteria that monoclinic phases must meet are listed in the supplementary material.[51] Here, we have selected the elastic constants calculated for the FM configuration using the 1x1x1 supercell of $FeNbO_4$ (P 2/c) to discuss our results and compare them to other types of ABO_4 materials in Table 2.

Table2 Elastic constants for monoclinic $FeNbO_4$, $HoNbO_4$ $LaNbO_4$ and $YTaO_4$.

Elastic constant	$FeNbO_4$ (P 2/c)	$HoNbO_4$ (P 2_1/c)[52]	$LaNbO_4$ (I 2/a)[53]	$YTaO_4$ (I_{12}/a1)[54]
C_{11} (GPa)	274.1	387.8	242.0	354.9
C_{22} (GPa)	269.8	292.3	177.0	291.9
C_{33} (GPa)	318.8	383.4	212.0	343.0
C_{44} (GPa)	74.5	44.6	43.9	88.1
C_{55} (GPa)	102.1	30.8	11.8	82.8
C_{66}(GPa)	57.1	51.9	53.6	73.5
C_{12} (GPa)	144.1	147.8	83.8	112.3
C_{13} (GPa)	148.5	194.9	185	146.1
C_{23} (GPa)	119.7	141.3	49.8	122.5
C_{15} (GPa)	-6.8	-35.3	4.1	1.0
C_{25} (GPa)	-11.7	-2.7	-16.4	-20.3
C_{35} (GPa)	-22.9	15.2	29.3	-57.5
C_{46} (GPa)	10.2	7.0	-8.9	-1.6

Few experimental studies of monoclinic ABO_4 structures have discussed elastic constants, and in Table 2 we have therefore compared with computational results on other monoclinic ABO_4 materials, which shows a similar trend. As regards parameters C_{11}, C_{22} and C_{33} which measure the stiffness along the a, b and c Cartesian directions, respectively, C_{22} (269.8 GPa) is smaller than both C_{11} (274.15 GPa) and C_{33} (318.86 GPa), indicating that m-$FeNbO_4$ is softer along the b direction, which is the same trend as seen in the $HoNbO_4$ (space group P 2_1/c) structure, where the values of C_{11}, C_{22} and C_{33} are 244.3 GPa, 231.2GPa and 272.1 Gpa, respectively[54]. As to C_{44}, C_{55} and C_{66}, which are linked to the shear deformation of the (100), (010) and (001) along the b, c and a directions, respectively, C_{66} has the lowest value (57.07 GPa), demonstrating that it is easier for the m-$FeNbO_4$ phase to shear in the (001) surface along the a direction than in the other two directions, which differs from the calculated results for $HoNbO_4$, $LaNbO_4$ (space group I 2/a) and YTaO4 (space group I_{12}/a1) where the value of C_{55} is the lowest[54-56]. Finally, C_{15}, C_{25} and C_{35} are associated with the shear strain in the x-z plane when adding a stress along the a, b and c directions in the (100), (010) and (001) surfaces, respectively. Their values are negative, which shows that the β angle will decrease when a tensile stress is applied along the a, b or c direction, which could be also seen in the monoclinic $HoNbO_4$, $LaNbO_4$ and $YTaO_4$ structures[52-54].

In a summary, we have demonstrated that the bulk properties would not be affected in a large degree by the spin direction of Fe^{3+} and thereby in order to simplify the calculations in the following section we would take 1x1x1 FM unit cell to build the surface models.

Simulation of the Low-Miller index surfaces

The m-$FeNbO_4$ lattice shows a high degree of asymmetry, as discussed above, and in order to identify the lowest energy and exposed surfaces for potential water adsorption and dissociation, it is necessary to consider all inequivalent low-Miller index facets. We have therefore calculated the surface energies of the different terminations of each of the 7 lowest Miller index surfaces, listed in Table 3. We also determined the type of surface terminations obtained, according to Tasker's method[55], which identifies three types of surfaces (type Ⅰ, Ⅱ, and Ⅲ), depending on the stacking of the planes of different types of atoms in an ionic crystal. In a type Ⅰ surface, the overall charge of each plane is zero due to its stoichiometric ratio of cations and anions, which makes it a non-polar surface. In a type Ⅱ surface, any dipole moments are cancelled out due to the symmetrical stacking of three charged planes. However, in a type Ⅲ surface, charged planes are stacked in an alternating sequence, which causes a net dipole moment perpendicular to the direction of the stacking of the planes. As a result, type Ⅰ or Ⅱ surfaces are stable and do not reconstruct, since there is no net dipole perpendicular to the stack direction within the stoichiometric repeat unit. A type Ⅲ surface, on the other hand, needs to be reconstruction to remove the net dipole, which we have achieved by moving half of the ions from the top layer to the bottom of slab to cancel out their dipole moments, thereby obtaining a surface slab with overall zero net dipole. From Table 3, we can see that the (100), (011) and (111) are type Ⅲ surfaces, which were therefore reconstructed through METADISE[30] to obtain a non-dipolar surface slab. In addition, the magnetic moments of Fe cations in the top layers decrease with respect to the 4.27 μ_B value simulated in the bulk, where the extent of the reduction is based on their reduced coordination number with the surrounding oxygen ions. For example, the fully-coordinated Fe cations in the (001) and (111) surface terminated with O have a larger magnetic moment (~4.22 μ_B) than in the (110) surface (4.05 μ_B), where only three oxygen ions are coordinating the Fe cations. Electrons remain in the undercoordinated Fe ion, thus causing the reduction of its magnetic moment.

Table 3 Surface energy and magnetic moment for the low-Miller index surfaces of $FeNbO_4$

Surface	Termination	Tasker type	Surface Energy (eV/nm^2)	μ_{Fe} (μ_B) on top layer
001	O	Ⅱ	5.27	4.22
010	O-Fe-O/O-Nb-O terminated	Ⅱ	1.97/4.41	4.10/-
100	Fe/Nb terminated	Ⅲ	7.23/13.25	4.05/-
011	Fe/Nb terminated	Ⅲ	3.47/7.51	4.13/4.15
101	O terminated	Ⅱ	4.54	4.18
110	Nb-O-Fe/O terminated	Ⅱ	3.32/4.02	4.19/4.19
111	O/Nb terminated	Ⅲ	3.08/4.54	4.21/4.17

The models of the simplest (001), (010) and (100) facets are shown in Figure 4. All slabs have the exposed atoms arranged regularly in the top and bottom layers. Nb and O form stronger bonds than Fe and O and, therefore, cleaving the surfaces with Nb in the top layers costs more energy than when Fe is in the top layers. For example, despite the Fe and Nb ions exposed in the top layer both having 3 dangling bonds in their two respective terminations of the (100) facet, the Nb termination has a larger surface energy of 13.25 eV/nm^2 compared to 7.23 eV/nm^2 for the Fe termination. Similarly, the (010) surface with the O-Fe-O termination has the lower energy of 1.97eV/nm^2 – and the lowest of the series of surface since there are only 2 dangling bonds per Fe atom – whereas the O-Nb-O termination also with 2 dangling bonds per Nb atom has a higher surface energy of 4.41 eV/nm^2. These results also highlight the impact of the number of dangling bonds in the top layer on the surface energies.

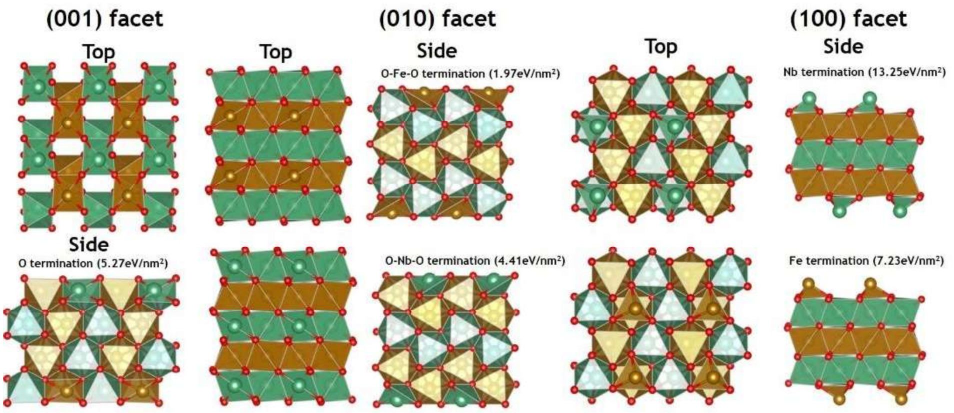

Figure 4 Model of the (001), (010) and (100) $FeNbO_4$ surfaces and their energies: O atoms are in red; Fe atoms are in yellow and Nb atoms are in green.

In the more complex (011), (101), (110) and (111) surfaces, which are presented in Figure 5, the atomic configuration is less regular than in the previously discussed surfaces. In the (011) facet, although there is a similar atomic arrangement in the two different terminations if we ignore the type of metal cation type, the surface terminated with Fe cations has a much lower surface energy (3.47 eV/nm^2) than the Nb terminated surface (7.51 eV/nm^2), since the Nb cations in the former plane have a larger coordination number than in the latter surface. This situation also occurs in the (111) facet, where there are more dangling bonds per Nb atom in the Nb termination (3.08 eV/nm^2) than in the O termination one (4.54 eV/nm^2), despite a similar atomic arrangement. In addition, for the (101) facet there is only one surface type with a surface energy of 4.54 eV/nm^2 and although it has the same atom coordination as the (011) Fe termination, the latter's surface energy is remarkably larger, due to the loose arrangement of atoms in the (101) surface. Surprisingly, the O termination of the (110) facet has a higher surface energy (4.02 eV/nm^2) than the Nb-O-Fe termination (3.32 eV/nm^2), despite having fewer dangling bonds, which reflects the impact of the atomic arrangement on the surface energies. For example, we would suggest that the existence of the zig-zag FeO_x-NbO_x chains in the top layer could maintain the structural stability of the surface.

To summarize, the atomic arrangement, the type of cation and number of dangling bonds in the top layers all affect the surface energy, which is therefore difficult to predict. The (010) surface with O-Fe-O termination has the lowest surface energy (1.97 eV/nm^2) within this group of low-Miller index surfaces, since it has a tight arrangement of surface atoms and only a few Fe-O dangling bonds.

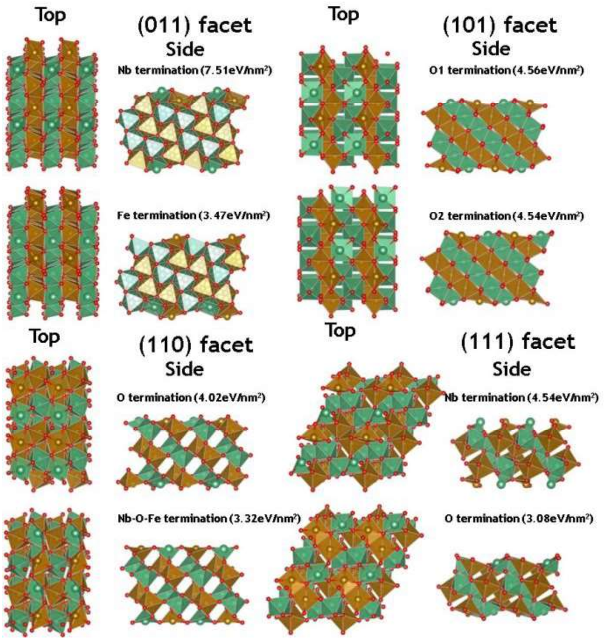

Figure 5 Model of the (011), (101), (110) and (111) $FeNbO_4$ surfaces and their energies: O atoms are in red; Fe atoms are in yellow and Nb atoms are in green.

Following the calculation of the surface energies and in order to explore which surfaces will be exposed in the nanoparticles of $FeNbO_4$ and have the potential to adsorb water, we constructed the Wulff morphology and calculated the STM images. Figure 6 shows the thermodynamic equilibrium crystal shape from the Wulff construction, which compares well with the particle morphology obtained experimentally[56] where FeNbO4 particles display the gem shape, and we are thus confident that our calculations are able to predict the correct relative surface stabilities. Figure 6 indicates that the main planes exposed in the nanoparticle are the (111), (110), (010) and (011) surfaces, with the (010) facet occupying the largest exposed area. As such, we only focus on these four major facets for the analysis of the STM images and the discussion of the water adsorption.

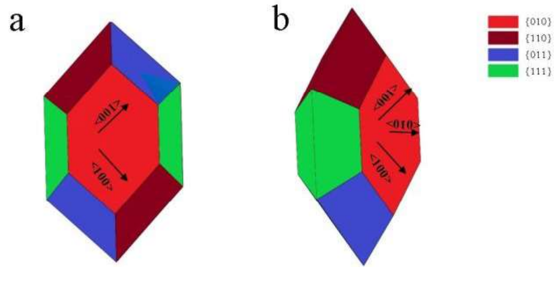

Figure 6 Different views of the equilibrium morphology of the $FeNbO_4$ crystal derived from a Wulff construction; a: vertical to <010> direction; b: side view.

Figure 7 shows the STM images of the $FeNbO_4$ (010), (011), (110) and (111) surfaces, where brightness represents height, i.e. the brighter the spot in the image, the closer is the ion to the STM probe tip. In the (010) surface, there is a distance of 1.30 Å between the topmost Nb and Fe ions, which are coordinated by four oxygen ions, two of which in the top layer and the other two in the sub-surface layer. The Fe ions lie above Nb and are therefore more exposed, making them good adsorption sites. In the (011) surface, Fe is clearly located in the top layer and is coordinated by two oxygen ions also in the top layer. The atom density and arrangement in the (110) surface is less packed than in the other three surfaces, which led to atomic rearrangements during optimization. In the (111) surface, more Fe cations with one dangling bond are exposed than Nb cations, whereas the Fe ions in the sub-surface layers are partially covered by the surrounding oxygen ions from the top surface layer.

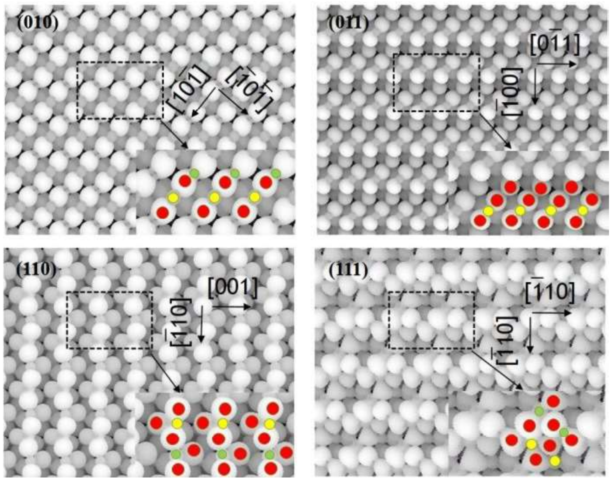

Figure 7 Scanning tunnelling microscopy (STM) images of the (010), (011), (110) and (111) $FeNbO_4$ surfaces: O atoms are in red; Fe atoms are in yellow and Nb atoms are in green.

Adsorption and dissociation of water at the surfaces

In this section, we explore the adsorption of water, followed by its dissocation, at the Fe and Nb surface sites in the four main $FeNbO_4$ surfaces expressed in the morphology, i.e. (011), (010), (110) and (111).

Fe site

The optimized adsorption structures and energies at 0 K are shown in Figure 8. We can see that after optimization, the water molecules remain located above the Fe cations in both the (011) and (010) surfaces. In addition, the bond length between the interacting oxygen in water and the Fe ion in the top layer of the (011) surface (O_w-Fe) is the smallest (~2 Å) and closest to the Fe-O bond in the FeO_6 octahedron in the bulk of $FeNbO_4$. However, the O_w-Fe distance at the other three surfaces has a larger value of almost 2.2 Å. The largest adsorption energies of -1.02 and -0.82 eV were calculated at the (011) and (010) surfaces, respectively, which can be explained based on the adsorption configuration with the water interacting closely with the surfaces.

To provide further information on the molecular adsorption, we have also plotted the charge transfer by calculating the charge density difference (Δρ) according to Eq (7):

$$\Delta\rho = \rho_{FeNbO_4-H_2O} - \rho_{FeNbO_4} - \rho_{H_2O} \qquad (7)$$

which is shown in Figure 8, where yellow color represents charge depletion and blue color represents charge gain. We found a clear charge transfer for all four surfaces with electron accumulation near the O_w-Fe bond, confirming the formation of this bond during adsorption, which is also consistent with the adsorption energy analysis.

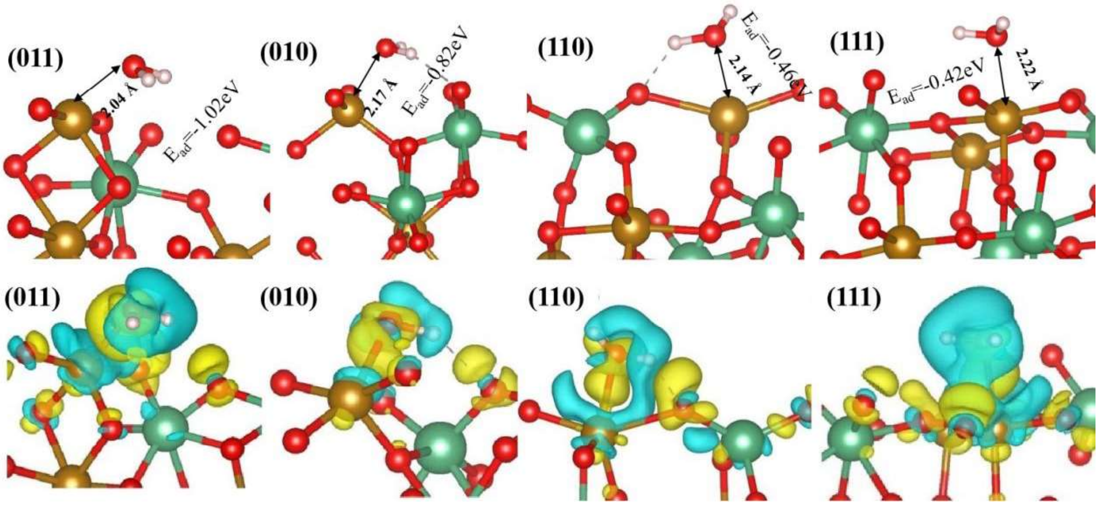

Figure 8 Most stable adsorption structures of H_2O on the Fe site of the $FeNbO_4$ (011), (010), (110) and (111) at 0 K and the related charge density difference: O atoms are in red; Fe atoms are in yellow and Nb atoms are in green.

We next analyzed the dissociation reaction pathways of the water molecule on the same four surfaces at 0, 300 and 600 K, shown in Figures 9 and S2. The values of zero point energy and vibrational entropy obtained from DFT calculations are listed in Tabe S3-5. The IS (initial state) represents the adsorption configuration where the surface-H_2O interface is formed. We found that all the adsorption energies increase as the temperature rises, indicating that it becomes more difficult for a water molecule to attach to the surfaces, a process that becomes endothermic at large temperatures. Once adsorbed on the surfaces, the energy barriers from IS to TS are essentially the same on each surface for all temperatures. Specifically, in the mechanisms studied, the adsorbed water molecule dissociates to form surface-bound –H and –OH groups (final state: FS). On the (011) and (010) surfaces, we note a similar reaction path, where the bond between H and OH in the water molecule is broken and the H attaches itself to the nearest surface O in the top layer, with both adsorbate fragments binding the same FeO_4 group. However, this reaction on the (010) surface has the largest free energy barrier ΔF_a = 2.6 eV, showing that the dissociation reaction is more difficult and less likely to proceed on the (010) surface than on the other three surfaces**.** On the (111) surface, the dissociation reaction pathway involves the H atom bonding the nearest surface O anion in the neighboring NbO_6 octahedron, with a barrier of 0.66 eV. On the (110) surface, a remarkable difference from the above three pathways is observed in the dissociation process. After adsorption of H_2O, the bridge between the FeO_4 and NbO_4 group in top layer is broken and the linking surface O anion moves towards its neighboring Nb cation. As a result, each H atom from the water molecule forms a hydrogen-bond with the surface O anion that used to connect the FeO_4 and NbO_4 groups, with an activation energy of just 0.16 eV, i.e. the smallest barrier observed for the four surfaces at 0 K. During the dissociation process, the H atom from the water molecule coordinates the former bridging oxygen atom, which now belongs to the NbO_6 octahedron. We can conclude that owing to the migration of the bridging O anion in the top layer and the formation of the hydrogen-bonds during the dissociation process, the (110) surface displays the most favorable pathway with the smallest barrier. In summary, the dissociation process on the (010) surface requires the largest energy to overcome the activation energy barrier, and the reaction on the (110) surface is therefore the most likely process to occur, since it requires the smallest activation free energy ΔF_a = 0.16 eV and the largest free energy for the dissociation reaction ΔF_{diss} = -0.43 eV.

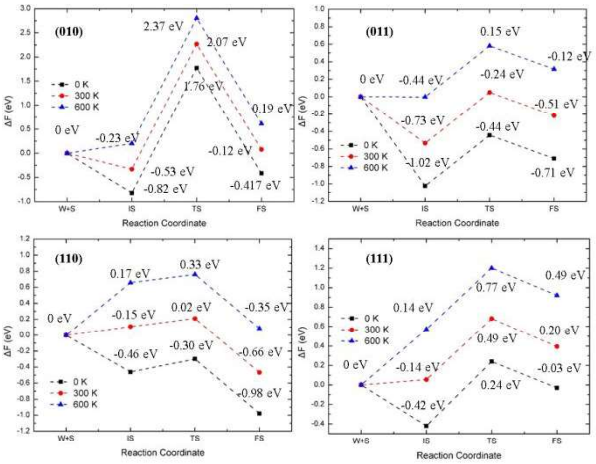

Figure 9 Water dissociation pathways in the $FeNbO_4$ (011), (010), (111) and (110) surfaces; W+S refers to isolated water molecule and surface; IS refers to initial state; TS refers to transition state; FS refers to final state.

Nb site

In this section, we investigated the reaction of a water molecule with the Nb cations in the top layer of the (011), (110) and (111) surfaces. Note that we did not consider this process on the (010) surface, since no Nb sites are exposed in the (010) surface. The adsorption structures after optimization at 0 K are shown in Figure 10, from which it is clear that on all three surfaces the bond distance between the water molecule and the Nb sites is longer than at the Fe sites discussed in the previous section. On both (011) and (111) surfaces, the exposed Nb cation coordinates five oxygen anions from the top surface layer and the dangling bond is used by the adsorbed water molecule, which has a similar position and distance of ~2.28 Å to the two facets. The adsorption energy of a water molecule binding to the (011) surface is -0.87 eV at 0 K, which is smaller than at the Fe site (-1.02 eV). Note that Nb has a larger Bader charge and we therefore should expect the interaction between Nb and O to be stronger than between Fe and O. However, we consider that these unexpectedly lower adsorption energies are caused by steric effects at the adsorption sites from the neighboring atoms. For example, despite both Fe and Nb having six-fold bulk coordination, the Fe cation in the (011) surface is coordinated by only four oxygen anions, making it a more available adsorption site than the Nb cation, which has a coordination number of five and is therefore less accessible for molecular adsorption. Moreover, for a similar arrangement of the surface O near the adsorption site, we found that the adsorption energy released at the Nb site is 0.02 and 0.78 eV larger than at the Fe site of the (110) and (111) surfaces at 0 K, respectively, despite the longer Nb-O bond distance compared to the Fe-O interaction.

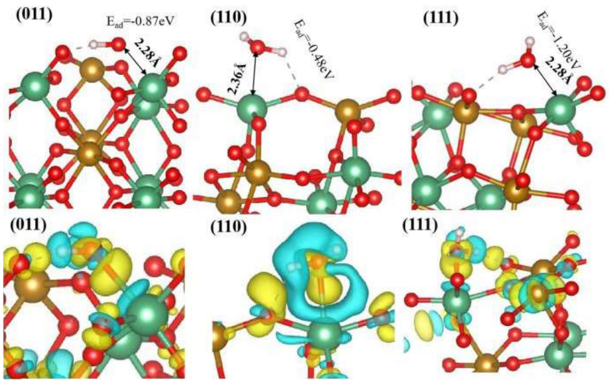

Figure 10 Most stable adsorption structures of H_2O on the Nb site of the $FeNbO_4$ (011), (110) and (111 at 0 K and the related charge density difference: O atoms are in red; Fe atoms are in yellow

and Nb atoms are in green.

To gain further insight into the interaction mechanism, we next calculated the charge transfers between the water molecules and surfaces, shown in Figure 10. Similar to the result at the Fe site, we found charge transfers between all the three surfaces and the water molecules, with the electron density accumulating near the interacting Nb-O_w bond.

Finally, we calculated the water dissociation pathways at the Nb site on the three surfaces, which are shown in Figure 11 and S3. Similar to the reactions on Fe site, our simulations also suggest that the adsorption becomes endothermic with the increment of temperature and after water dissociation the H migrates and attaches to the nearest O in the top surface layer. We also found that during water dissociation on the (110) surface, the system only needs to overcome a very small activation energy barrier of 0.27 eV at 0 k, compared to a barrier of 0.82 eV on the (011) surface and 0.36 eV on the (111) surface. Our calculations indicate that the water dissociation reaction on the (110) surface releases 0.43 eV of energy at 0 K, whereas this process on the other two surfaces is endothermic, requiring 0.53 eV and 0.12 eV, respectively. Unlike the process at the Fe site, the dissociation pathway at the Nb site on the (110) surface, does not induce the migration of the bridging O towards the Nb cation. In summary, the water dissociation reaction at the Nb site of the (110) surface is the most easily achieved with the smallest activation free energy value ΔF_a = 0.27 eV and the largest free energy for the dissociation reaction ΔF_{diss} = -0.423eV.

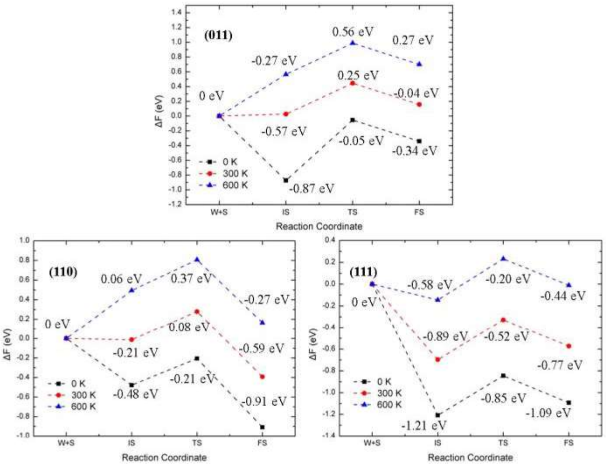

Figure 11 Water dissociation pathway in the $FeNbO_4$ (011), (110) and (111) surface; W+S refers to isolated water molecule and surface; IS refers to initial state; TS refers to transition state; FS

refers to final state.

Conclusions

In this work, we have carried out a comprehensive computational study of the bulk and surface properties of the monoclinic phase of $FeNbO_4$, including the adsorption and dissociation reaction of water on its surfaces. The optimized bulk structure shows a typical monoclinic lattice with a unique axis b (β=90.4°) where the Fe cations stay in a high spin state with a magnetization of 4.27 μ_B. The Bader charge of the Nb cations is larger than for the Fe atoms, which explains the stronger Nb-O bond compared to the Fe-O bond. The PDOS plot explains that the electron conduction takes place through the Fe-O-Fe sub-lattice, which is consistent with the experimental results. The calculated elastic constants meet all the stability conditions for the monoclinic phase.

The (010) facet has the lowest surface energy and occupies the largest area in the Wulff construction morphology, where the (011), (110) and (111) facets are also exposed. The surfaces terminated with Nb cations with four- or three-fold oxygen coordination have the largest surface energy, owing to the strong Nb-O bond.

Finally, we studied the adsorption and dissociation reaction of a water molecule at the Fe and Nb sites exposed in the four surfaces expressed in the morphology. For all surfaces, the adsorption reaction will turn into endothermal with the increment of Temperature and, the most favorable water adsorption takes place at the Nb site of the (111) surface and at the Fe site of the (011) surface, realising adsorption energies of -1.17 and -1.00 eV, respectively. The dissociation of water at both the Fe and Nb sites could be achieved most easily on the (110) surface, which also displays the lowest activation energy barriers at 0 K, supporting the feasibility of this process.

Acknowledgements

Xingyu Wang acknowledges the China Scholarship Council (CSC) [No. 201906460008] and the

University of Leeds for a PhD scholarship. This work has used the computational facilities of the Advanced Research Computing at Cardiff (ARCCA) Division, Cardiff University and HPC Wales, and the high performance computing facilities (ARC4) provided by the University of Leeds. We also acknowledge computing resources on the the UK's national supercomputing service ARCHER facility (http://www.archer.ac.uk) via our membership of the UK's HEC Materials Chemistry Consortium, which is funded by EPSRC (EP/L000202).

Conflicts of Interest: None.

Author Contribution Statement

Xingyu Wang, David Santos-Carballal, and Nora H. de Leeuw conceived of the presented idea. David Santos-Carballal, and Nora H. de Leeuw developed the theory and performed the computations and Xingyu Wang carried out the computational experiments and wrote the manuscript with support from David Santos-Carballal, and Nora H. de Leeuw. In addition, Nora H. de Leeuw supervised the project.

TOC:

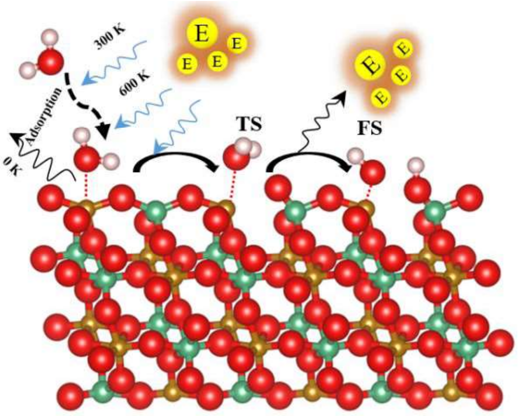

References

.1. Zhang, H.; Kim, Y. K.; Jeong, H. Y.; Lee, J. S., A Few Atomic $FeNbO_4$ Overlayers on Hematite Nanorods: Microwave-Induced High Temperature Phase for Efficient Photoelectrochemical Water Splitting. *ACS Catal.* **2018**, *9*, 1289-1297.

2. Liu, X.; Xie, D.; Irvine, J. T. S.; Ni, J.; Ni, C., An $FeNbO_4$-Based Oxide Anode for a Solid Oxide Fuel Cell (Sofc). *Electrochim. Acta* **2020**, *335*, 135692.

3. Devesa, S.; Graça, M. P.; Henry, F.; Costa, L. C., Dielectric Properties of Fenbo4 Ceramics Prepared by the Sol-Gel Method. *Solid State Sci.* **2016**, *61*, 44-50.

4. Wang, T.; Shi, S.; Kong, F.; Yang, G.; Qian, B.; Yin, F., The Role of Stable Interface in Nano-Sized $FeNbO_4$ as Anode Electrode for Lithium-Ion Batteries. *Electrochim. Acta* **2016**, *203*, 206-212.

5. Liu, X.; Zhou, J.; Xie, D.; Ni, J.; Ni, C., Fenbo4-Based Oxide Cathode for Steam Electrolysis. *Solid State Sci.* **2020**, *345*, 115181.

6. Ananta Supon; Brydson Rik; W., T., Synthesis, Formation and Characterisation of Fenbo4 Powders. *J. Eur. Ceram. Soc.* **1998**, *19*, 489-496.

7. Theissmann, R.; Ehrenberg, H.; Weitzel, H.; Fuess, H., Domain Structure and Lattice Strains in $FeNbO_4$. *Solid State Sci.* **2005**, *7*, 791-795.

8. Leiva, H.; Sieber, K.; Khazai, B.; Dwight, K.; Wold, A., Structural and Electronic Relationships between Conducting Iron Niobates and Iron Tungstates. J. *Solid State.* **1980**, *35*, 128-132.

9. Ehrenberg, H.; Wltschek, G.; Theissmann, R.; Weitzel, H.; Fuess, H.; Trouw, F., The Magnetic Structure of Fenbo4. *J. Magn. Magn. Mater.* **2000**, *218*, 261-265.

10. M., H. V.; HK., M.-B., Fenb04: Untersuchungen an Einkristallen Rnit Wolf Ramit- Und $AINbO_4$-Struktur. *Z. anorg. allg. Chem* **1979**, 456, 99-105.

11. Kanti Biswas Soumya; Gnanasekaran, T.; Kumar Ghorai, T.; Pramanik, P., Sensing Properties of Chemically Synthesized Pristine and Ptimpregnated Nanosized Fenbo4 in Hydrogen, Ammonia, and Lpg. *J. Electrochem. Soc.* **2008**, *155*, J26-J31.

12. Dawson, D. H.; Williams, D. E., Gas-Sensitive Resistors: Surface Interaction of Chlorine with Semiconducting Oxides. *J. Mater. Chem.* **1996**, *6*, 409-414.

13. Babu, R.; Kelkar, S.; Kashid, V.; Achary, S. N.; Salunke, H. G.; Gupta, N. M., Photophysical, Bandstructural, and Textural Properties of O- $FeNbO_4$ in Relation to Its Cocatalyst-Assisted Photoactivity for Water Oxidation. *RSC Adv.* **2014**, *4*, 33435-33445.

14. Jones, B. M. F.; Maruthamani, D.; Muthuraj, V., Construction of Novel N-Type Semiconductor Anchor on 2d Honey Comb Like $FeNbO_4$/Rgo for Visible Light Drive Photocatalytic Degradation of Norfloxacin. *J. Photochem. Photobiol., A* **2020**, *400*, 112712.

15. Ahmed, S. H.; Bakiro, M.; Alzamly, A., Visible-Light-Driven Photocatalytic Formation of Propylene Carbonate Using Fenbo4/Reduced Graphene Oxide Composites. *Materialia* **2020**, *12*, 100781.

16. Ni, C.; Feng, J.; Cui, J.; Zhou, J.; Ni, J., Ann-Type Oxide $Fe_{0.5}Mg_{0.25}Ti_{0.25}Nb_{0.9}Mo_{0.1}O_{4-\delta}$ for Both Cathode and Anode of a Solid Oxide Fuel Cell. *J. Electrochem. Soc.* **2017**, *164*, F283-F288.

17. Goodenough, J. B.; Huang, Y.-H., Alternative Anode Materials for Solid Oxide Fuel Cells. *J. Power Sources* **2007**, *173*, 1-10.

18. Deka, D. J.; Gunduz, S.; Fitzgerald, T.; Miller, J. T.; Co, A. C.; Ozkan, U. S., Production of Syngas

with Controllable H_2/Co Ratio by High Temperature Co-Electrolysis of CO_2 and H_2O over Ni and Co-Doped Lanthanum Strontium Ferrite Perovskite Cathodes. *Appl. Catal., B* **2019**, *248*, 487-503.

19. Yu, J.; Men, H. J.; Qu, Y. M.; Tian, N., Performance of Ni-Fe Bimetal Based Cathode for Intermediate Temperature Solid Oxide Electrolysis Cell. *Solid State Sci.* **2020**, *346*, 115203.

20. Trini, M.; Jørgensen, P. S.; Hauch, A.; Bentzen, J. J.; Hendriksen, P. V.; Chen, M., 3d Microstructural Characterization of Ni/YSZ Electrodes Exposed to 1 Year of Electrolysis Testing. *J. Electrochem. Soc.* **2019**, *166*, F158-F167.

21. Hubert, M.; Laurencin, J.; Cloetens, P.; Morel, B.; Montinaro, D.; Lefebvre-Joud, F., Impact of Nickel Agglomeration on Solid Oxide Cell Operated in Fuel Cell and Electrolysis Modes. *J. Power Sources* **2018**, *397*, 240-251.

22. Kresse, G.; Hafner, J., Ab Initio Molecular Dynamics for Open-Shell Transition Metals. *Phys. Rev. B: Condens. Matter.* **1993**, *48*, 13115-13118.

23. Kresse, G.; Hafner, J., Norm-Conserving and Ultrasoft Pseudopotentials for First-Row and Transition Elements. *J. Phys.: Condens. Matter* **1994**, *6*, 8245-8260.

24. Kresse, G.; Furthmiiller, J., Efficiency of Ab-Initio Total Energy Calculations for Metals and Semiconductors Using a Plane-Wave Basis Set. *Comput. Mater. Sci.* **1996**, *6*, 15-20.

25. Kresse, G.; Furthmuller, J., Efficient Iterative Schemes for Ab Initio Total-Energy Calculations Using a Plane-Wave Basis Set. *Phys. Rev. B: Condens. Matter.* **1996**, *54*, 11169-11186.

26. Blochl, P. E., Projector Augmented-Wave Method. *Phys. Rev. B: Condens. Matter.* **1994**, *50*, 17953-17979.

27. Perdew, J. P.; Burke, K.; Ernzerhof, M., Generalized Gradient Approximation Made Simple. *Phys. Rev. Lett.* **1996**, *77*, 3865-3868.

28. Dudarev, S. L.; Botton, G. A.; Savrasov, S. Y.; Humphreys, C. J.; Sutton, A. P., Electron-Energy-Loss Spectra and the Structural Stability of Nickel Oxide: An Lsda□u Study. *Phys. Rev. B* **1998**, *57*, 1505-1509.

29. Henkelman, G.; Arnaldsson, A.; Jónsson, H., A Fast and Robust Algorithm for Bader Decomposition of Charge Density. *Comput. Mater. Sci.* **2006**, *36*, 354-360.

30. Watson, G. W.; Kelsey, E. T.; de Leeuw, N. H.; Harris, D. J.; Parker, S. C., Atomistic Simulation of Dislocations, Surfaces and Interfaces in Mgo. *J. Chem. Soc., Faraday Trans.* **1996**, *92*, 433-438.

31. Santos-Carballal, D.; Roldan, A.; Grau-Crespo, R.; de Leeuw, N. H., A Dft Study of the Structures, Stabilities and Redox Behaviour of the Major Surfaces of Magnetite Fe(3)O(4). *Phys. Chem. Chem. Phys.* **2014**, *16*, 21082-97.

32. Santos-Carballal, D.; Cadi-Essadek, A.; de Leeuw, N. H., Catalytic Conversion of Co and H2 into Hydrocarbons on the Cobalt Co(111) Surface: Implications for the Fischer–Tropsch Process. *J. Phys. Chem. C* **2021**, *125*, 11891-11903.

33. Ye, X.; Jiang, X.; Chen, L.; Jiang, W.; Wang, H.; Cen, W.; Ma, S., Effect of Manganese Dioxide Crystal Structure on Adsorption of So2 by Dft and Experimental Study. *Appl. Surf. Sci.* **2020**, *521*.

34. Ungerer, M. J.; Santos-Carballal, D.; Cadi-Essadek, A.; van Sittert, C.; de Leeuw, N. H., Interaction of H2o with the Platinum Pt (001), (011), and (111) Surfaces: A Density Functional Theory Study with Long-Range Dispersion Corrections. *J. Phys. Chem. C :Nanomater Interfaces* **2019**, *123*, 27465-27476.

35. Graeme, H.; P., U. B.; Hannes, J. n., A Climbing Image Nudged Elastic Band Method for Finding Saddle Points and Minimum Energy Paths. *J. Chem. Phys.* **2000**, *113*, 9901-9904.

36. C., L. D.; Jorge, N., On the Limited Memorybfgs Method for Large Scale Optimization.

Mathematical Programming **1989**, *45*, 503-528.

37. Ying, Y.; Fan, K.; Luo, X.; Huang, H., Predicting Two-Dimensional Pentagonal Transition Metal Monophosphides for Efficient Electrocatalytic Nitrogen Reduction. *J. Mater. Chem. A* 2019, 7, 11444-11451.

38. A. A. Peterson, F. A.-P., F. Studt, J. Rossmeisl and J. K. Nørskov, How Copper Catalyzes the Electroreduction of Carbon Dioxide into Hydrocarbon Fuels. *Energy Environ. Sci. 2*010, 3, 1311-1315.

39. Burgess R. Donald, Jr., " Thermochemical Data " in NIST Chemistry WebBook, NIST Standard Reference Database Number 69, Eds. P.J. Linstrom and W.G. Mallard, National Institute of Standards and Technology, Gaithersburg MD, 20899, https://doi.org/10.18434/T4D303, (retrieved August 5, 2021).

40. Wulff, G., Zur Frage Der Geschwindigkeit Des Wachsthums Und Der Auflösung Der Krystallflächen. Zeitschrift Für Kristallographie. *Crystalline Materials* **1901**, *34*, 1-6.

41. Santos-Carballal, D.; Roldan, A.; Grau-Crespo, R.; de Leeuw, N. H., A Dft Study of the Structures, Stabilities and Redox Behaviour of the Major Surfaces of Magnetite Fe(3)O(4). *Phys. Chem. Chem. Phys.* **2014**, *16*, 21082-97.

42. Boateng, I. W.; Tia, R.; Adei, E.; Dzade, N. Y.; Catlow, C. R.; de Leeuw, N. H., A Dft+U Investigation of Hydrogen Adsorption on the $LaFeO_3$(010) Surface. *Phys. Chem. Chem. Phys.* **2017**, *19*, 7399-7409.

43. Dzade, N. Y.; de Leeuw, N. H., Periodic Dft+U Investigation of the Bulk and Surface Properties of Marcasite (FeS_2). *Phys. Chem. Chem. Phys.* **2017**, *19*, 27478-27488.

44. Vanpoucke, D. E. P.; Brocks, G., Formation of Pt-Induced Ge Atomic Nanowires on Pt/Ge(001): A Density Functional Theory Study. *Phys. Rev. B* **2008**, *77*, 241308.

45. Tersoff, J.; Hamann, D. R., Theory and Application for the Scanning Tunneling Microscope. *Phys. Rev. Lett.* **1983**, *50*, 1998-2001.

46. Lakshminarasimhan, N.; Kumar, A. K. N.; Chandrasekaran, S. S.; Murugan, P., Structure-Magnetic Property Relations in $FeNbO_4$ Polymorphs: A Spin Glass Perspective. *Prog. Solid State Chem.* **2019**, *54*, 20-30.

47. Ahmed, S. H.; Bakiro, M.; Alzamly, A., Effect of Ph and Surfactant on Band Gap Properties of Monoclinic $FeNbO_4$ Prepared Via Different Routes. *Nano-Struct. Nano-Objects.* **2019**, *20*, 100400.

48. E., S.; J., S., Electrical Resistivity, Thermopower, and 57 Fe Mössbauer Study of $FeNbO_4$. *J. Solid State Chem.* **1997**, *134*, 253-264.

49. Roldan, A.; Santos-Carballal, D.; de Leeuw, N. H., A Comparative DFT Study of the Mechanical and Electronic Properties of Greigite Fe_3S_4 and Magnetite Fe_3O_4. *J. Chem. Phys.* **2013**, *138*, 204712.

50. Devey, A. J.; Grau-Crespo, R.; de Leeuw, N. H., Combined Density Functional Theory and Interatomic Potential Study of the Bulk and Surface Structures and Properties of the Iron Sulfide Mackinawite (Fes). *Journal of Physical Chemistry C* **2008**, *112*, 10960-10967.

51. Wu, Z.-j.; Zhao, E.-j.; Xiang, H.-p.; Hao, X.-f.; Liu, X.-j.; Meng, J., Crystal Structures and Elastic Properties of Super hard IrN2 and IrN3 from First Principles. *Phys. Rev. B* **2007**, *76*, 054415.

52. Garg, A. B.; Errandonea, D.; Rodriguez Hernandez, P.; Munoz, A., High-Pressure Monoclinic-Monoclinic Transition in Fergusonite-Type Honbo4. *J. Phys. Condens. Matter.* **2021**, 33, 195401-195415.

53. S, F. E., Elastic Moduli and Acoustic Symmetry of Ferroelastic LaNbO4 and BiVO4. *Journal of Physics: Condensed Matter*, *1*, 2875-2890.

54. Feng, J.; Shian, S.; Xiao, B.; Clarke, D. R., First-Principles Calculations of the High-Temperature Phase Transformation in Yttrium Tantalate. *Phys. Rev. B* **2014**, *90*,094102.

55. Tasker, P. W., The Stability of Ionic Crystal Surfaces. *Journal of Physics C: Solid State Sci.* **1979**, *12*, 4977−4984.

56. Wanklyn, B. M., Flux Growth of Some Complex Oxide Materials. *J. Mater. Sci.* **1972**, *7*, 813-821.